On the dynamics and survival of fractal clouds in galactic winds

W. E. Banda-Barragán,[1,2]⋆ F. Zertuche,[1] C. Federrath,[3] J. García Del Valle,[1] M. Brüggen,[2] and A. Wagner[4]

[1]*Facultad de Ingeniería Civil y Mecánica, Universidad Técnica de Ambato, Av. Los Chasquis y Río Payamino S/N, Ambato 180206, Ecuador*
[2]*Hamburger Sternwarte, Universität Hamburg, Gojenbergsweg 112, D-21029 Hamburg, Germany*
[3]*Research School of Astronomy and Astrophysics, Australian National University, Canberra, ACT 2611, Australia*
[4]*Center for Computational Sciences, University of Tsukuba, 1-1-1 Tennodai, Tsukuba, Ibaraki 305-8577, Japan*

ABSTRACT

We report the results of a series of hydrodynamical simulations of supersonic winds interacting with quasi-isothermal fractal clouds in the interstellar medium. We investigate how the initial variance of the log-normal density field influences the morphology, dynamics, and survival of wind-swept clouds. We compare uniform, solenoidal, and compressive fractal cloud models in both 3D and 2D configurations. In both geometries we find that the processes of disruption and entrainment of interstellar clouds in supersonics winds are both functions of the initial probability density function in the cloud. In a general context fractal clouds accelerate faster and mix earlier than uniform clouds. In the context of fractal clouds compressive wind-swept clouds are more confined, less mixed, and less accelerated than their solenoidal counterparts. Despite their slower bulk speeds, compressive clouds are also less prone to Kelvin-Helmholtz and Rayleigh-Taylor instabilities, so they survive longer and reach larger distances than solenoidal clouds before they are destroyed. These results show that entrainment of dense gas in winds is more efficient in compressive cloud models than in solenoidal cloud models, thus making clouds in the compressive regime ideal testbeds for future cloud acceleration studies with self-consistent velocity and magnetic fields. The diagnostics reported in this paper show numerical convergence at the standard resolutions, and the results hold for differently-seeded and distinctly-oriented fractal clouds.

Key words: MHD – ISM: magnetic fields – ISM: clouds – methods: numerical – turbulence – galaxies: starburst

1 INTRODUCTION

Multi-wavelength observations of star-forming galaxies reveal that galactic winds are large-scale, multi-phase outflows characterised by several gas, dust, and cosmic-ray components. Galactic winds have a hot ($\sim 10^7$ K), ionised phase that moves at speeds of $500 - 1500 \, \text{km s}^{-1}$, plus a cold ($\sim 10^2 - 10^4$ K), atomic/molecular phase that moves at speeds of $50 - 200 \, \text{km s}^{-1}$. A current, open problem in the theory of galactic winds is understanding how dense gas in the cold phase survives in the hot outflow and how it reaches high latitudes ($\sim 100 - 1500 \, \text{pc}$ above and below the galactic planes). Two theories have been proposed to explain the presence of cold, dense clouds and filaments in galactic winds. The first one relies on momentum-driven acceleration as the mechanism to transport clouds from low to high latitudes, whilst the second one relies on thermal instabilities as the trigger for the in-situ formation of clouds at high latitudes.

In the first scenario clouds near the galactic planes of galaxies are advected from low to high latitudes by either the ram pressure, the radiation pressure, or the cosmic-ray pressure of the outflowing material. A challenge of this scenario is explaining how dense clouds survive the disruptive effects of pressure gradients and dynamical instabilities to become entrained in the wind. In the second scenario, the hot gas in the outflowing wind cools down as it moves outwards and becomes thermally unstable in the process, thus triggering the formation of dense clouds at high latitudes via clumping. For this scenario to work, however, the wind needs to be sufficiently mass loaded at the launching site. Thus, the question remains open and the parameter space to explore in all models is still broad to draw definite conclusions. The reader is referred to for a recent review of galactic wind models.

In this paper we concentrate on the first of the above-mentioned scenarios and study clouds that are being ram-pressure accelerated by supersonic winds. We use hydrodynamical, numerical simulations to study wind-cloud models in a previously-unexplored parameter space: one in which turbulent density profiles are considered

⋆ E-mail: wlady.bsc@gmail.com (WBB)

for the initial cloud set-ups. Wind-cloud and shock-cloud problems have been widely studied in recent years (see a full list of the parameters explored by previous authors in Appendix A). In most previous models, none the less, clouds have been idealised as spherical clumps of gas with either uniform or smoothed density profiles. In this idealised scenario, numerical hydrodynamical (hereafter HD) models show that adiabatic clouds are disrupted by instabilities before they travel large distances, while radiative and thermally-conducting clouds survive longer but are not effectively accelerated. These results indicate that entrainment is not effective in such models.

Despite the above conclusion, the parameter space in models with magnetic and/or turbulent clouds has been less explored. When included, however, both magnetic fields and turbulence have been shown to produce significant effects on the morphology, dynamics, and survival of wind-swept clouds. On the one hand, numerical magnetohydrodynamical (hereafter MHD) models show that clouds threaded by either uniform, tangled, or turbulent magnetic fields are further clumped and more protected against dynamical instabilities than their uniform counterparts. The extra magnetic pressure at shearing layers reduces vorticity generation, but the clouds are not effectively accelerated unless the wind is also strongly magnetised. In such case, the effective drag force acting upon the cloud is enhanced, aiding cloud acceleration. On the other hand, cloud models with supersonic velocity fields and/or strong, turbulent magnetic fields also favour scenarios in which clouds undergo a period of fast acceleration. In these models the initial turbulent kinetic and magnetic energy thermalises, thus allowing the cloud to expand, accelerate, and reach high velocities without being significantly disrupted by dynamical instabilities, e.g., Kelvin-Helmholtz (KH) and Rayleigh-Taylor (RT) instabilities.

These results indicate that cloud entrainment could be effective if magnetic fields and turbulence are taken into account in wind-cloud models in a self-consistent manner. However, in previous papers only comparisons between uniform and fractal/turbulent clouds were carried out without considering changes in the probability density function (hereafter PDF) of the density field associated with distinct regimes of turbulence. For instance, in our paper we only tested clouds characterised by a single PDF. Thus, in this paper we explore the effects of varying the initial density PDF of turbulent clouds between two extreme regimes of turbulence, namely solenoidal and compressive. We do not include supersonic velocity fields or tangled magnetic fields in this paper as we are interested in isolating the effects of changing the initial statistical parameters of the log-normal density field upon the morphology, dynamics, and survival of clouds embedded in hot, supersonic winds.

The remainder of this paper is organised as follows. In section 2 we report details on the code and diagnostics we use for our simulations. In section 3 we present 2D plots and curves that contrast our different wind-cloud scenarios. In section 4 we summarise our findings.

2 METHOD

2.1 Simulation code

In order to carry out the simulations reported in this paper, we use the PLUTO v4.0 code (see Mignone et al. 2007) in 3D (X_1, X_2, X_3) and 2D (X_1, X_2) cartesian coordinate systems. We solve the system of mass, momentum, and energy conservation laws of ideal hydrodynamics (HD) using the HLLC approximate Riemann solver of

Miyoshi & Kusano (2005) jointly with a Courant-Friedrichs-Lewy (CFL) number of $C_a = 0.3$. The conservation laws read:

$$\frac{\partial \rho}{\partial t} + \boldsymbol{\nabla} \cdot [\rho \boldsymbol{v}] = 0, \tag{1}$$

$$\frac{\partial [\rho \boldsymbol{v}]}{\partial t} + \boldsymbol{\nabla} \cdot [\rho \boldsymbol{v} \boldsymbol{v} + \boldsymbol{I} P] = 0, \tag{2}$$

$$\frac{\partial E}{\partial t} + \boldsymbol{\nabla} \cdot [(E + P) \boldsymbol{v}] = 0, \tag{3}$$

$$\frac{\partial [\rho C]}{\partial t} + \boldsymbol{\nabla} \cdot [\rho C \boldsymbol{v}] = 0, \tag{4}$$

where ρ is the mass density, $\boldsymbol{v}$ is the velocity, $P = (\gamma - 1) \rho \epsilon$ is the gas thermal pressure, $E = \rho \epsilon + \frac{1}{2} \rho v^2$ is the total energy density, ϵ is the specific internal energy, and C is a Lagrangian scalar used to track the evolution of gas initially contained in the cloud.

The simulations presented in this paper have been designed as scale-free wind-cloud models. Thus, instead of explicitly including radiative cooling as a source term in the above numerical scheme, we approximate the effects of energy losses in the gas by using a soft adiabatic index of $\gamma = 1.1$ for all the models.

2.2 Initial and boundary conditions

2.2.1 *Dimensionless set-up*

Our simulation sample comprises 22 models split into 2 sets of runs: a 3D set and a 2D set. The 3D set includes 2 models with turbulent clouds and the 2D set includes 20 models with fractal clouds. In both sets, the simulation set-up consists of a single turbulent or fractal cloud with radius r_{cloud} and average density ρ_{cloud}, embedded in a supersonic wind with density, ρ_{wind}, and Mach number:

$$\mathcal{M}_{\text{wind}} = \frac{|\boldsymbol{v_{\text{wind}}}|}{c_{\text{wind}}} = 4.9, \tag{5}$$

where $|\boldsymbol{v_{\text{wind}}}| \equiv v_{\text{wind}}$ and $c_{\text{wind}} = \sqrt{\gamma \frac{P_{\text{th}}}{\rho_{\text{wind}}}}$ are the speed and sound speed of the wind, respectively. In all models the density contrast between wind and cloud material is:

$$\chi = \frac{\rho_{\text{cloud}}}{\rho_{\text{wind}}} = 10^3 \tag{6}$$

2.2.2 *3D turbulent cloud models*

In the 3D set, we initialise the clouds with log-normal density fields taken from snapshots of simulations of solenoidal and compressive turbulence reported by (see model ...). We set-up two models, 3DSol and 3DComp, with solenoidal and compressive clouds, respectively, by following a four-step process: 1) we mask regions in the clouds domain outside a radius r_{cloud}; 2) we scale the average density to ρ_{cloud} in both clouds, 3) we interpolate the resulting density data cube into the 3D simulation domain described below, and 4) we initialise the simulations with the clouds in thermal pressure equilibrium (P) with the ambient medium. This process allows us to compare the evolution of both models and ensure that all simulations start with clouds of the same initial mass and average density.

2.2.3 3D domain and resolution

The 3D turbulent clouds are centred in the origin $(0, 0, 0)$ of the computational domain, which consists of a prism with a spatial range $-5\,r_{\text{cloud}} \leq X_1 \leq 5\,r_{\text{cloud}}$, $-2\,r_{\text{cloud}} \leq X_2 \leq 28\,r_{\text{cloud}}$, and $-5\,r_{\text{cloud}} \leq X_3 \leq 5\,r_{\text{cloud}}$. The numerical resolution is R_{64} (i.e., 64 cells cover the cloud radius), which corresponds to a uniform grid resolution of $(N_{X_1} \times N_{X_2} \times N_{X_3}) = (640 \times 1920 \times 640)$. This resolution is adequate to describe the overall evolution of 3D turbulent cloud models as shown in our previous paper for a similar configuration.

2.2.4 2D fractal cloud models

The above-mentioned 3D models are computationally expensive, so we can only investigate wind.-cloud models in small simulation domains at the resolution required for convergence. This means that we can only follow the evolution of 3D wind-swept clouds for a couple of dynamical time-scales before a significant amount of cloud mass leaves the computational domain. Therefore, in order to follow the evolution of solenoidal and compressive cloud models for longer time-scales and larger spatial scales, we also investigate in this paper 2D wind-cloud models in these two regimes of turbulence..

In the 2D set, we also initialise the clouds with density profiles described by log-normal distributions, but in this set we generate these scalar fields using the pyFC library instead of taking snapshots from previous simulations. We configure two sets of models, 2DSol and 2DComp, each representing 10 solenoidal and 10 compressive clouds, respectively, by following a four-step process: 1) we use the pyFC library to iteratively produce 512^2-sized data cubes with different seeds containing clouds with log-normal density distributions with variances and fractal dimensions characteristic of solenoidal and compressive clouds; 2) we mask regions in the fractal cloud domain outside a radius r_{cloud}; 3) we scale the average density of each cloud to ρ_{cloud} so that all models start with the same mass and initial mean density; 4) we interpolate the clouds into the simulation domain described below and initialise the simulations with the wind and cloud in thermal pressure equilibrium.

2.2.5 2D domain and resolution

In the 2D set, the cloud is also centred in the origin $(0, 0)$ of the computational domain, which consists of a rectangular area with a spatial range $-40\,r_{\text{cloud}} \leq X_1 \leq 40\,r_{\text{cloud}}$, $-2\,r_{\text{cloud}} \leq X_2 \leq 158\,r_{\text{cloud}}$. The numerical resolution is R_{128} (128 cells cover the cloud radius), which corresponds to a uniform grid resolution of $(N_{X_1} \times N_{X_2} \times N_{X_3}) = (640 \times 1920 \times 640)$. This resolution is adequate to describe the overall evolution of 2D uniform cloud models as shown in, and in Section of this paper.

Figure 1 shows the initial clouds in the 3D set and two of the models in the 2D set, one solenoidal model and one compressive model. Table 1 presents a summary of the models described above.

2.2.6 Boundary conditions

In both sets (2D and 3D) we prescribe diode boundary conditions on the lateral and back sides of the simulation domains and an inflow boundary condition on the front side. The inflow zone is located at the ghost zone that faces the leading edge of the cloud and injects a constant supply of wind gas into the computational domain.
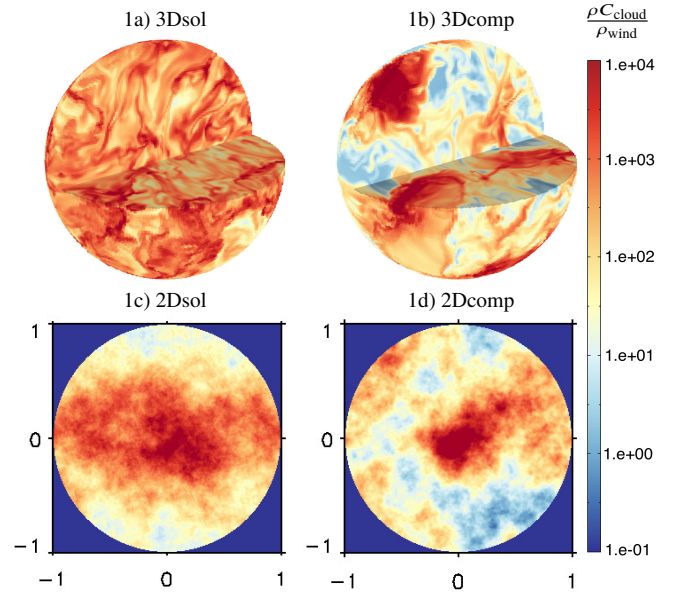
Figure 1. Initial density structure and PDFs of the fractal clouds reported in this paper.

2.3 Diagnostics

To compare the results from different simulations we use mass-averaged quantities:

$$\langle \mathcal{G} \rangle = \frac{\int \mathcal{G} \rho\, C\, dV}{M_{\text{cloud}}} = \frac{\int \mathcal{G} \rho\, C\, dV}{\int \rho\, C\, dV}, \tag{7}$$

where G is any scalar from the simulation, V represents the volume, C is the cloud tracer defined in Section 2.1, and M_{cloud} is the total mass of the cloud.

2.3.1 Morphological diagnostics

Using Equation (7), we define the effective radii along each axis $(j = 1, 2, 3)$[1] as:

$$\iota_{\text{j,cloud}} = \left[5 \left(\langle X^2_{\text{j,cloud}} \rangle - \langle X_{\text{j,cloud}} \rangle^2 \right) \right]^{\frac{1}{2}}, \tag{8}$$

where $\langle X_{\text{j,cloud}} \rangle$ and $\langle X^2_{\text{j,cloud}} \rangle^{1/2}$ are the average cloud position and its rms, respectively. Thus, the lateral width of the cloud along X_1 reads $\iota_{\text{1,cloud}}$ and the displacement of its centre of mass along the streaming axis X_2 reads $\langle X_{\text{2,cloud}} \rangle$. Henceforth, these quantities are normalised with respect to the initial cloud radius, r_{cloud}.

2.3.2 Dynamical diagnostics

In a similar fashion, we define the dispersion of the j-component of the velocity, $\delta_{\text{v}_{\text{j,cloud}}}$, as:

$$\delta_{\text{v}_{\text{j,cloud}}} = \left(\langle v^2_{\text{j,cloud}} \rangle - \langle v_{\text{j,cloud}} \rangle^2 \right)^{\frac{1}{2}}, \tag{9}$$

---

[1] Note that in 2D simulations we only have two axes, so j = 1, 2.

Table 1. Initial conditions for the 3D and 2D models. Column 1 provides the name of the model set, column 2 indicates the number of runs in each set, columns 3 and 4 show the normalised domain size and the numerical resolution in terms of cells per cloud radius, columns 5 and 6 show the polytropic index and wind Mach number, column 7 shows the type of cloud density field, and columns 8 and 9 report the cloud-to-wind density contrast and the normalised standard deviation of the initial cloud densities.

(1)	(2)	(3)	(4)	(5)	(6)	(7)	(8)	(9)
Model	Runs	Domain	Resolution	γ	$\mathcal{M}_{\text{wind}}$	Density Field	χ	$\frac{\sigma_{\rho_{\text{cloud}}}}{\rho_{\text{cloud}}}$
3Dunif	1	$(10 \times 30 \times 10)\, r_{\text{cloud}}$	R_{64}	1.1	4.9	Uniform	10^3	0
3Dsol	1	$(10 \times 30 \times 10)\, r_{\text{cloud}}$	R_{64}	1.1	4.9	Fractal	10^3	1.3
3Dcomp	1	$(10 \times 30 \times 10)\, r_{\text{cloud}}$	R_{64}	1.1	4.9	Fractal	10^3	4.1
2Dsol	10	$(80 \times 160)\, r_{\text{cloud}}$	R_{128}	1.1	4.9	Fractal	10^3	1.9
2Dcomp	10	$(80 \times 160)\, r_{\text{cloud}}$	R_{128}	1.1	4.9	Fractal	10^3	5.9

where $\langle\, v_{\text{j,cloud}}\,\rangle$ and $\langle\, v_{\text{j,cloud}}^2\,\rangle^{1/2}$ are the average cloud velocity and its rms, respectively. Based on these quantities, the cloud bulk velocity reads $\langle\, v_{2,\text{cloud}}\,\rangle$ and the transverse velocity dispersion reads $\delta_{v_{\text{cloud}}} \equiv |\boldsymbol{\delta_{v_{\text{cloud}}}}| = (\sum_j \delta_{v_{\text{j,cloud}}}^2)^{1/2}$ for j = 1, 3. Henceforth, these quantities are normalised with respect to the wind speed, v_{wind}.

2.3.3 Mass-loss diagnostics

In order to understand cloud disruption and how gas with different densities evolve, we measure the fraction of gas mixing occurring between cloud and wind material using the following definition:

$$f_{\text{mix}_{\text{cloud}}} = \frac{\int \rho\, C_{\text{mix}}\, dV}{M_{\text{cloud},0}}, \tag{10}$$

where the numerator represents the mass of cloud gas mixed with the wind, $0.1 \leq C_{\text{mix}} \leq 0.9$ is the tracer tracking mixed gas, and $M_{\text{cl},0}$ is the initial mass of the cloud.

In addition, we define cloud mass fractions at or above a density threshold, $\rho_{\text{threshold}}$, as:

$$F_{1/\text{threshold}} = \frac{M_{1/\text{threshold}}}{M_{\text{cloud},0}} = \frac{\int [\rho\, C]_{\rho \geq \rho_{\text{threshold}}}\, dV}{M_{\text{cloud},0}}, \tag{11}$$

where $M_{1/\text{threshold}}$ is the total mass of cloud gas with densities at or above a density threshold. Using Equation (11) we define $F_{1/500}$, $F_{1/100}$, $F_{1/10}$, $F_{1/3}$, and F_1, as the fractions of cloud mass with densities at or above $\rho_c/500$, $\rho_c/100$, $\rho_c/10$ $\rho_c/3$, and ρ_c, respectively.

2.4 Reference time-scales

The dynamical time-scales relevant for the simulations presente here are:

a) The cloud-crushing time (see Jones et al. 1994, 1996),

$$t_{\text{cc}} = \frac{2r_{\text{cloud}}}{v_{\text{shock}}} = \left(\frac{\rho_{\text{cloud}}}{\rho_{\text{wind}}}\right)^{\frac{1}{2}} \frac{2r_{\text{cloud}}}{\mathcal{M}_{\text{wind}}c_{\text{wind}}} = \chi^{\frac{1}{2}} \frac{2r_{\text{cloud}}}{\mathcal{M}_{\text{wind}}c_{\text{wind}}}, \tag{12}$$

where $v_{\text{shock}} = \mathcal{M}_{\text{wind}}\, c_{\text{wind}}\, \chi^{-\frac{1}{2}}$ is the approximate speed of the shock refracted into the cloud after the initial wind-cloud collision. Henceforth, we use the cloud-crushing time to normalise all time-scales[2].

---

[2] Note that in some previous studies authors used the cloud radius rather than its diameter to definite the cloud-crushing time. Thus, if the reader wishes to compare our time-scales to such studies, the definition needs to

b) The KH instability growth time (see Chandrasekhar 1961):

$$t_{\text{KH}} \simeq \frac{\chi_{\text{eff}}^{1/2}}{k_{\text{KH}}\, (v'_{\text{wind}} - v'_{\text{cloud}})}, \tag{13}$$

where $k_{\text{KH}} = \frac{2\pi}{\lambda_{\text{KH}}}$ is the wavenumber of the KH perturbations and the primed quantities of the physical variables correspond to their values at the location of shear layers.

c) The RT instability growth time (see Chandrasekhar 1961):

$$t_{\text{RT}} \simeq \frac{1}{[k_{\text{RT}}\, (a_{\text{eff}})]^{1/2}}, \tag{14}$$

where $k_{\text{RT}} = \frac{2\pi}{\lambda_{\text{RT}}}$ is the wavenumber of the RT perturbations. Note that both Equations (13) and (14) were originally derived for incompressible fluids, so any KH and RT time-scales reported hereafter should be considered solely as indicative values for the models reported in this paper.

d) The simulation time depends on whether the models are 3D or 2D. In the 3D set the simulation time is $t_{\text{sim}}/t_{\text{cc}} = 2.5$, while in the 2D set the simulation time is $t_{\text{sim}}/t_{\text{cc}} = 8.0$.

3 RESULTS

3.1 Overall cloud evolution

The disruption process of quasi-isothermal clouds immersed in supersonic winds occurs in a similar fashion in uniform and turbulent/fractal cloud models (see also). In both cases clouds are disrupted in 4 stages, but their resulting morphology, dynamics, and destruction time-scales differ depending on their initial density distributions. We highlight the main qualitative similarities and differences in the evolution of uniform and turbulent/fractal cloud models below:

(i) In the first stage the initial impact of the wind on the cloud triggers both reflected and refracted shocks. The reflected shock creates a bow shock at the leading edge of the cloud while the refracted shock travels through the cloud at speed, v_{shock} (see the left-hand side plane of Figure 3). In turbulent/fractal cloud models the bow shock is anisotropic and several refracted shocks (instead of a single shock) are transmitted to the cloud (see the mid- and right-hand side plane of Figure 3). This is because the density fields in turbulent/fractal clouds have a more intricate substructure than uniform density fields.

be contrasted with ours and, if needed, all the times reported in this paper should be multiplied by a factor of 2.
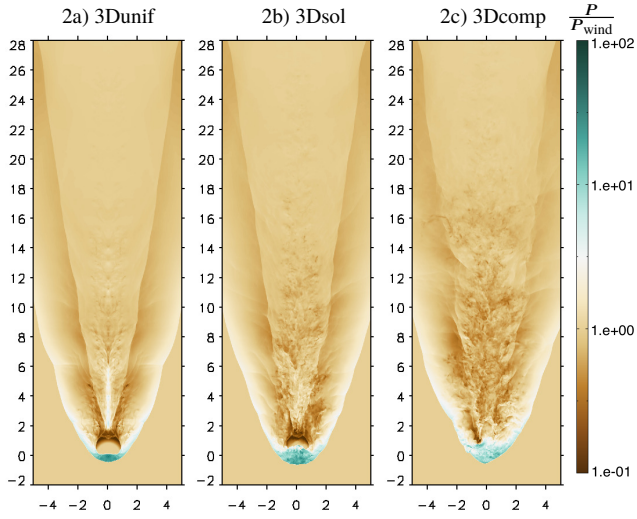
Figure 2. 2D slices at $X_3 = 0$ of the 3D uniform (left-hand side panel), and 3D fractal solenoidal (middle panel) and compressive (right-hand side panel) cloud models showing the normalised pressure profile at $t/t_{cc} = 0.5$. In fractal cloud models, an anisotropic bow shock forms at the leading edge of the cloud and several refracted shocks travel through the cloud, in contrast to the symmetric bow shock and the single refracted shock characteristic of the uniform cloud model.

(ii) In the second stage the cloud expands as a result of internal shock heating and pressure-gradient forces start to accelerate it downstream. In general, shock-driven expansion increases the effective cross sectional area of clouds and facilitates the wind-to-cloud momentum transfer. However, this occurs differently for turbulent/fractal and uniform cloud models. Turbulent/fractal clouds are porous, so they expand and accelerate faster than uniform clouds because the wind can more easily remove (and move through) low-density regions in them.

(iii) In the third stage acceleration continues and the cloud loses mass via stripping by KH instabilities. KH instabilities mainly grow at the sides of the clouds at locations where velocity shears occur. Vortical motions remove gas from the cloud and the wind deposits it downstream, thus forming a long-standing filamentary tail at the rear side of the cloud. In turbulent/fractal cloud models wind and cloud gas mix more effectively than in uniform models, so the resulting filament has a more complex structure populated by a collection of knots and sub-filaments.

(iv) In the fourth stage the cloud has accelerated sufficiently for RT instabilities to grow at the leading edge of it, so the cloud/filament breaks up into smaller cloudlets and tails as RT bubbles penetrate the cloud. These cloudlets and tails survive for a few extra dynamical time-scales before fully dissolving into the ambient medium. Fractal/turbulent and uniform cloud models experience break-up phases differently. While the break-up of uniform clouds is abrupt, turbulent/fractal clouds undergo a rather steady disruption process as they have several nuclei and each of them undergoes its own break-up phase at its own time-scale.

3.2 The role of the initial density PDF

As discussed in the previous section, the initial density distribution of clouds influences their evolution. Both the uniform and fractal clouds in our sample are initialised with the same mass and average

density, however, they evolve into filaments that are morphologically and dynamically different. These differences translate into uniform and fractal clouds being accelerated and disrupted at different rates. As we discuss throughout this paper, the same occurs when we consider subsamples of fractal clouds with different statistical descriptors. For simplicity we study the disruption of subsamples of fractal clouds in 2 regimes of turbulence, namely solenoidal and compressive. Figures 6 and 5 show the evolution of the 3D and 2D sets of fractal cloud models, respectively.

3.2.1 Solenoidal versus compressive cloud models

Figure 6 shows 2D midplane slices of the cloud density (ρC) in 3D models, at 5 different times in the range $0.5 \leq t/t_{cc} \leq 2.5$. Panel A of this figure shows the evolution of the solenoidal cloud model, while panel B shows the evolution of the compressive cloud model. The sub-panels underneath each panel show the time evolution of the density PDFs, normalised with respect to the initial cloud density, in each regime. All these panels show that solenoidal clouds are more expanded, travel faster, lose high-density gas more quickly, and are disrupted earlier than their compressive counterparts.

These differences can be understood if we compare the evolution of the PDFs of solenoidal and compressive cloud models. The solenoidal cloud has a PDF with a low variance. The low-density tail of the PDF in this model is rapidly flattened, while the high-density tail dissolves over short time-scales $\sim t/t_{cc} = 1.5$. On the contrary, the compressive cloud starts with a high variance, and even though the low-density tail of the PDF does flatten at very early stages, the high-density tail moves much slower towards lower values than in the solenoidal case. In fact, the high-density gas in the compressive model only dissolves at $t/t_{cc} = 2.5$ and acts as a long-lived footpoint for the downstream filament.

The analysis above indicate that the process of cloud disruption is indeed sensitive to the initial cloud substructure, but it does not allow us to conclude yet that the differences seen in the models are tied to the initial variances of the PDFs. For example, the explanation could be that the mass in the compressive model is arranged in such a way that high-density gas is somewhat protected from the wind by upstream gas that prevents it from been ablated, thus delaying its disruption. However, as we show below the differences seen in 3D solenoidal and compressive cloud models can actually be linked to initial density variance.

3.2.2 A statistical view of solenoidal and compressive clouds

Models in 3D are computationally expensive, so using a 3D geometry constrains both the size of the computational domain and the number of realisations that we can investigate. Thus, we will now look into a 2D set of solenoidal and compressive fractal cloud models. Analysing 2D models allows us to enlarge the computational domain, increase the simulation sample, and build up statistics on the behaviour of solenoidal and compressive cloud models, at a fraction of the computational resources needed for a similar 3D study.

We run 20 fractal cloud models in 2D, 10 of which are representative of the solenoidal regime and 10 of the compressive regime. Each of the clouds in each regime is generated with a different seed, so it has a different spatial distribution of densities than its pairs, but the same log-normal statistical parameters. Since the cloud evolution depends on the initial density distribution, each cloud has its own intrinsic evolution. However, we find that clouds that
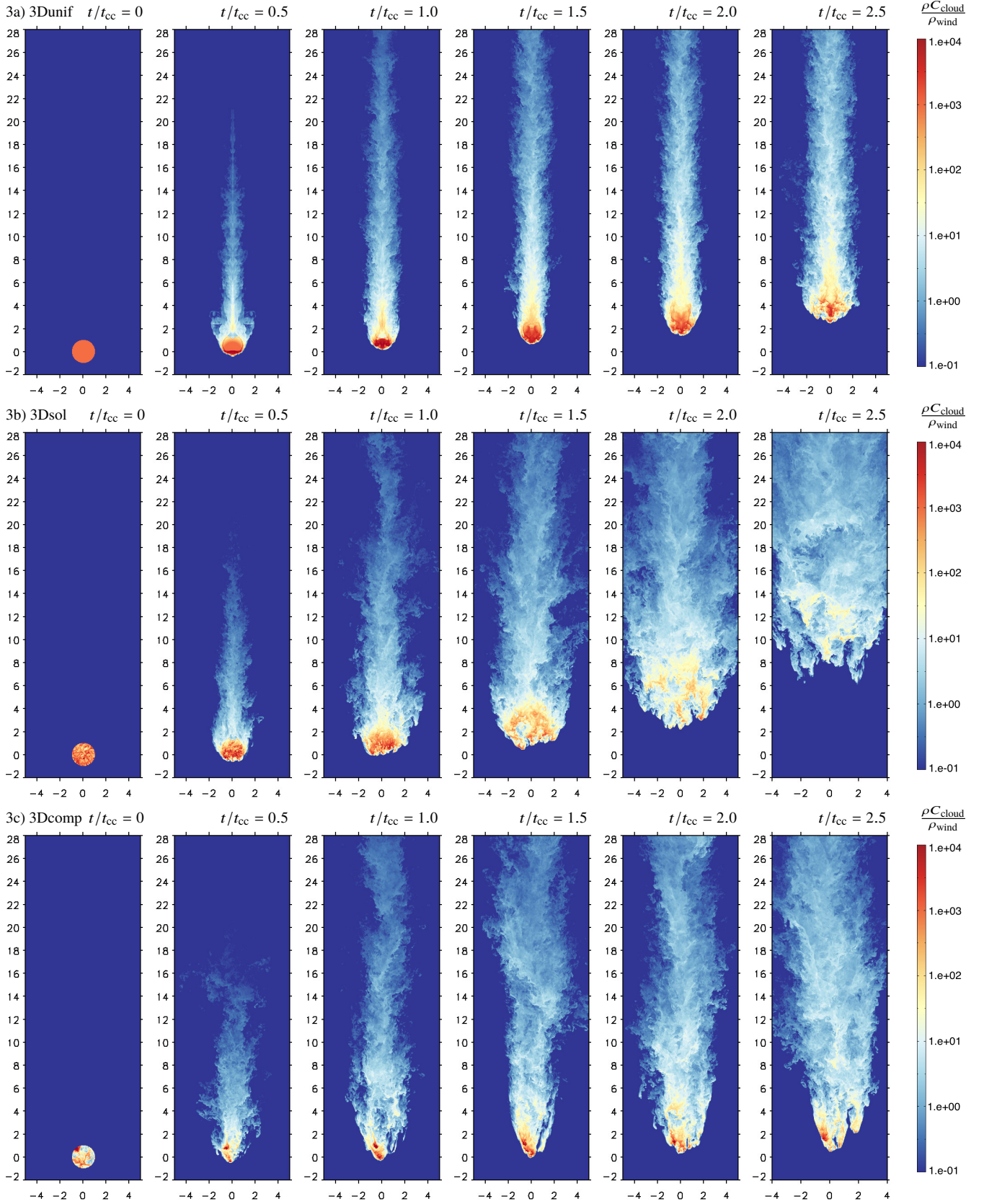
Figure 3. 2D plots showing the evolution between $1 \leq t/t_{cc} \leq 8$ of the cloud gas density (ρC_{cloud}) for two 2D models, sole2d and comp2d, that are representative of the solenoidal (Panel A) and compressive (Panel B) regimes, respectively. The cloud that starts off with a higher variance is slower and more confined than its low-variance counterpart, as it is supported by a higher density core.
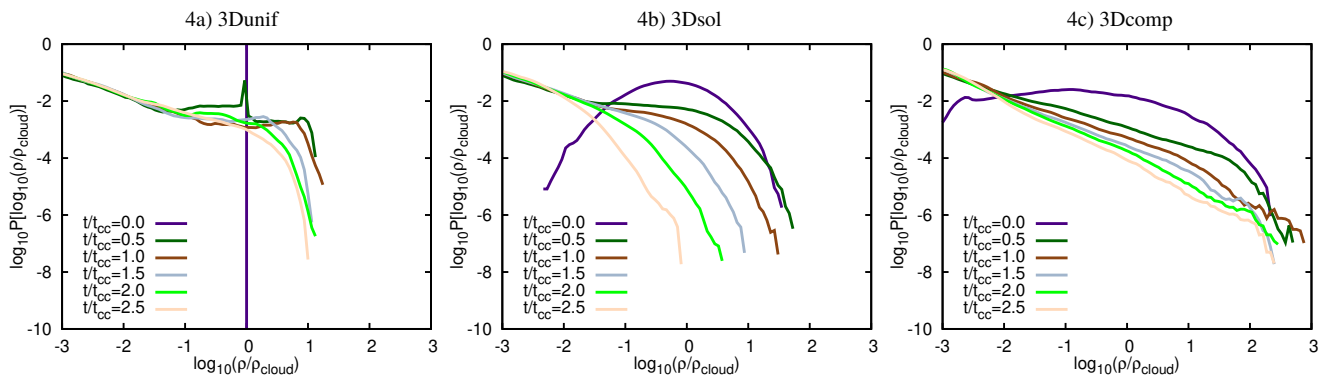
Figure 4. Time evolution of four diagnostics: the lateral width (top, left-hand side panel), the mixing fraction (top, right-hand side panel)), the displacement of the cloud's centre of mass (bottom, left-hand side panel), and the cloud's bulk speed (bottom, right-hand side panel) in models 2d-sole, 2d-comp, 3d-sole, and 3d-comp. The cloud with a high initial variance is both more collimated and slower than its counterparts. Mixing in the compressive models occur earlier.

are initialised with the same log-normal density parameters, either solenoidal or compressive, do display common, regime-dependent morphological and dynamical features.

In this context , Figure 5 shows 2D representations of the cloud density (ρC) in 2D models, at 5 different times in the range $1 \leq t/t_{cc} \leq 8$. Panel A of this figure shows the evolution of a fiducial solenoidal model from the 2D sample, while panel B shows the evolution of a fiducial compressive model. The sub-panels underneath each panel show the time evolution of the density PDFs, normalised with respect to the initial cloud density, in each regime.

These panels confirm the conclusions drawn from the analysis of the 3D runs, i.e., that solenoidal clouds have larger cross sections, higher accelerations, and are disrupted faster than their compressive counterparts. The sub-panels showing the evolution of the PDFs also display features seen in the 3D models. The high-density tail in the compressive cloud moves towards low-density values slower than in the solenoidal case, thus indicating that clouds in the compressive regime are disrupted over longer time-scales than clouds in the solenoidal regime.

3.3 Cloud morphology and dynamics

To quantify the morphological and dynamical differences in the evolution of solenoidal and compressive cloud models, we study the evolution of 4 diagnostics. Figure **??** presents the time evolution of the lateral width (panel A), displacement of the centre of mass (panel B), bulk speed (panel C), and acceleration (panel D) of both 3D and 2D fractal cloud models. The curves corresponding to 3D models are displayed independently, while the curves corresponding to 2D models are grouped and represented by the mean with a solid line and the $\pm 1\,\sigma$ limits with shaded areas around the mean. We confirm the qualitative results discussed above and find that the dynamics of clouds is strongly coupled to their morphology. In addition, the results from both 3D and 2D models are consistent with each other and show similar trends.

Panel A shows that, in average, solenoidal clouds are more expanded than compressive clouds with differences becoming more accentuated after $t/t_{cc} = 1$ in both 3D and 2D models. The lower variance of solenoidal density fields allows the internal shocks to move through, heat up, and expand the clouds faster than in the compressive cases. The end result is that solenoidal cloud models produce downstream tails that are on average ∼ 80 per cent less confined than compressive models.

Panels B, C, and D show the dynamical evolution of clouds. The wind can more readily percolate through porous clouds than through solid or uniform clouds, so the downstream tails in fractal models have more complex kinematics. Since the transfer of momentum from the wind to the cloud is more effective when clouds have larger cross sectional areas, we find that solenoidal clouds can be more effectively accelerated than compressive clouds. This means that solenoidal clouds can reach larger distances and acquire higher bulk speeds than their compressive counterparts, over the same time-scales.

3.4 Gas mixing and dispersion

Understanding how the cloud gas is mixed and dispersed into the ambient medium is another important aspect of wind-cloud interactions. Figure **??** presents the time evolution of the velocity dispersion (panel E) and mixing fraction (panel F) of both 3D and 2D fractal cloud models. Both panels show that on average solenoidal clouds are more turbulent (i.e. have higher velocity dispersions) and mix faster with ambient medium than compressive clouds. The processes of mixing and dispersion of gas in wind-swept clouds are associated with the generation of vortical motions in it via KH instabilities. Since the effective cloud radius in compressive cloud models is smaller than in solenoidal cloud models, the growth of KH instabilities is delayed in such models.

For comparison we compute the ratio of the KH instability growth time-scales for solenoidal and compressive clouds at $t/t_{cc} = 2$. We find that that KH instabilities with wavelengths comparable to r_{cloud} grow x times slower in the compressive models than in the solenoidal models. This explains why gas mixing is less efficient and why the downstream tails are less turbulent in compressive models when compared to solenoidal models.

3.5 Mass loss and cloud destruction

The efficiency of gas mixing has a direct impact on cloud destruction, i.e., on how much of the original cloud mass is left in the cloud after certain time. The destruction time of wind-swept clouds has been defined somewhat arbitrarily in the literature. A common practice to define cloud destruction has been to set a density threshold and designate all gas with densities at or above that threshold as cloud. Since the cloud mixes with its surroundings, the amount of
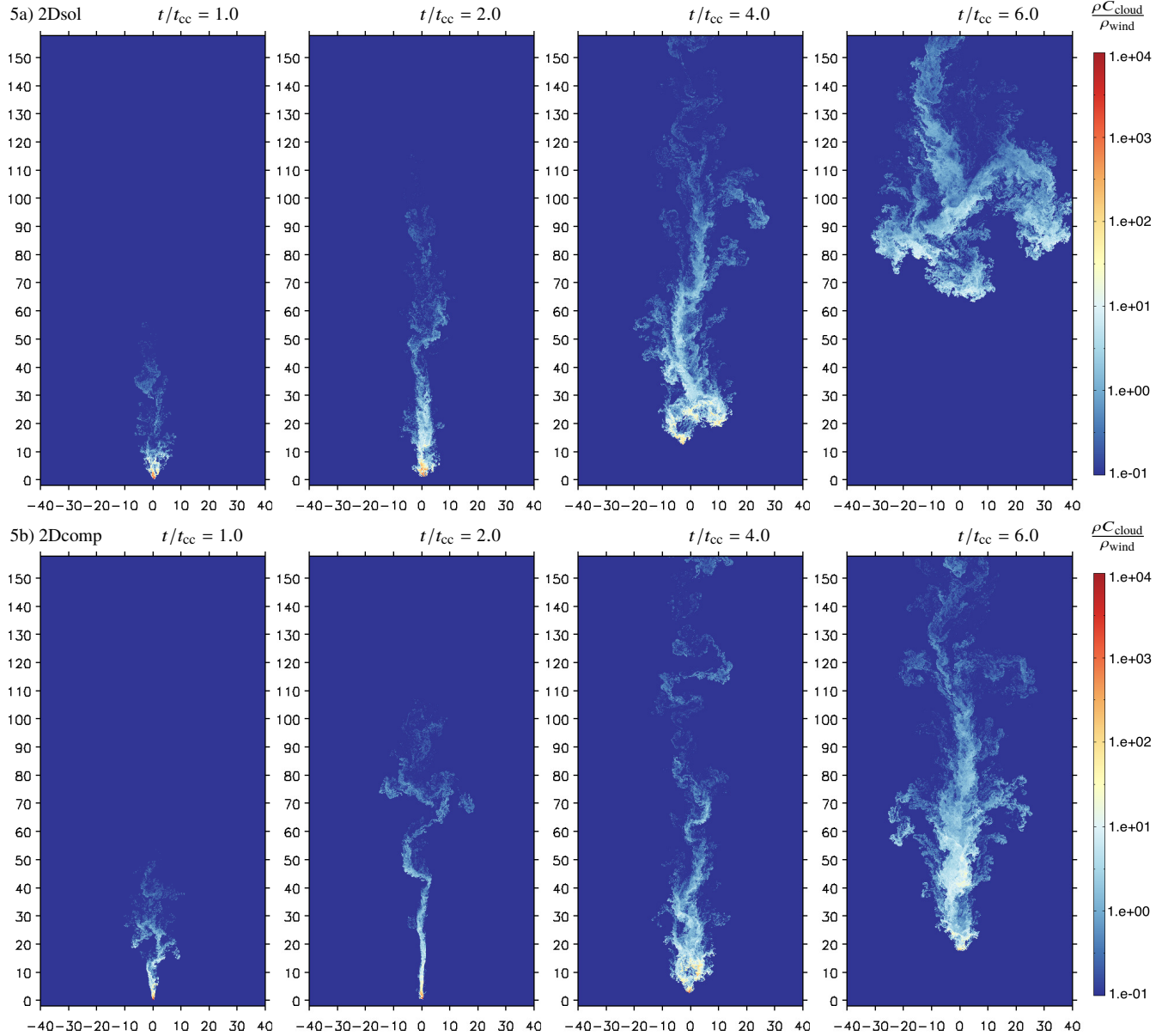
Figure 5. 2D plots showing the evolution between $1 \leq t/t_{cc} \leq 8$ of the cloud gas density (ρC_{cloud}) for two 2D models, sole2d and comp2d, that are representative of the solenoidal (Panel A) and compressive (Panel B) regimes, respectively. The cloud that starts off with a higher variance is slower and more confined than its low-variance counterpart, as it is supported by a higher density core.

cloud gas with high densities goes down until only a small percentage of it can still be qualified as cloud material. When the percentage of cloud mass goes below that percentage, the cloud is considered destroyed.

In order to compare our models with the results from previous works, we compute the fractions of cloud mass above different density thresholds. By doing this, we are also able to study the evolution and dynamics of cloud gas at different densities. Figure 7 presents the both the time evolution (left-hand side panels) and spatial evolution (right-hand side panels) of cloud mass fractions at or above the following density thresholds: $F_{1/500}$, $F_{1/100}$, $F_{1/10}$, $F_{1/3}$, and F_1. We define our clouds as destroyed when $F_{1/3} = 20$ per cent of the initial cloud mass, i.e., when only 20 per cent of the

initial cloud mass has densities above 1/3 of the original average density in the cloud.

The panels of Figure 7 reveal that in both 3D and 2D models:

(i) Compressive clouds lose mass at a lower rate than solenoidal clouds regardless of the reference density threshold being considered.

(ii) As the density threshold goes up, the difference between solenoidal and compressive models becomes more accentuated.

(iii) On average, compressive clouds are destroyed x times later than solenoidal clouds.

(iv) The dynamics of low-density gas in solenoidal and compressive models is similar, i.e., low-density gas in both regimes travels similar distances over the same dynamical time-scales.
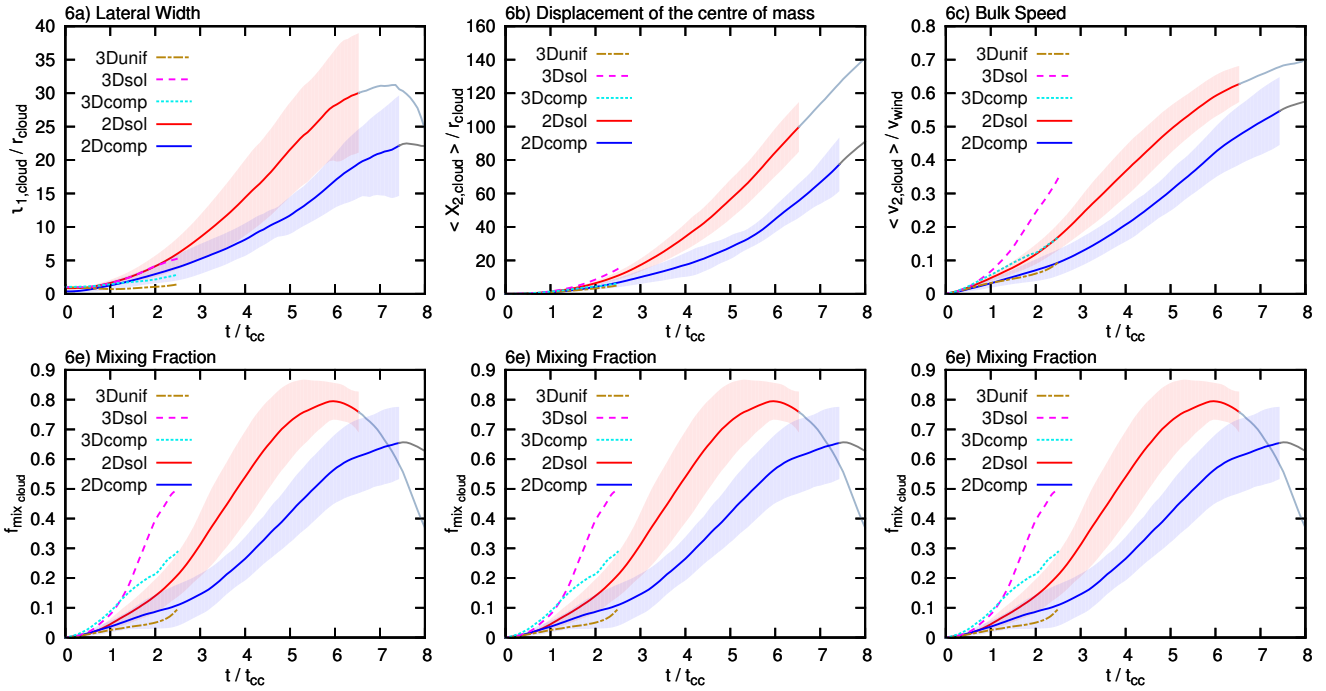
Figure 6. Time evolution of four diagnostics: the lateral width (top, left-hand side panel), the mixing fraction (top, right-hand side panel)), the displacement of the cloud's centre of mass (bottom, left-hand side panel), and the cloud's bulk speed (bottom, right-hand side panel) in models 2d-sole, 2d-comp, 3d-sole, and 3d-comp. The cloud with a high initial variance is both more collimated and slower than its counterparts. Mixing in the compressive models occur earlier.

(v) As the density threshold goes up, the difference between solenoidal and compressive models becomes more accentuated.

(vi) By the time clouds are destroyed, compressive clouds have travelled distances that are on average 1.25 times larger than solenoidal clouds

3.6 Cloud entrainment

We have seen that the evolution of dense gas in solenoidal and compressive models is different. In general, the high-density gas in compressive models survives longer and reaches larger distances than in solenoidal models, but is the entrainment of dense in the wind efficient? To respond this question we will now look into kinematics of clouds in the 2 regimes.

Figure 7 shows mass-weighted histograms of velocity of the cloud as a function of its density. These maps allow us to study how efficient is entrainment of cloud gas in different density bins. We find that gas with densities of $> x$ can reach speeds of the order of, while gas with higher densities can only reach speeds. Entrainment of high-density gas in compressive models is more efficient than in solenoidal models, however, in both cases the speed acquired by the high-density gas before it is destroyed is only a fraction of the wind speed, implying that the entrainment of high-density gas in the wind is overall not efficient.

3.7 Resolution effects

In order to asses how our choice of numerical resolution affects the evolution of fractal clouds, we present an extra set of simulations of two models at varying resolutions (see Table **??**). Figure **??** presents 3 panels showing the displacement of the centre of mass, the velocity dispersion, and the mass fraction $F_{1/3}$ of 2 fractal clouds

representative of solenoidal and compressive turbulence regimes. We find that the standard resolutions of R_{64} in 3D and R_{128} are adequate to describe the morphological and dynamical evolution of fractal clouds.

4 CONCLUSIONS

We have reported the results from a systematic numerical study, in both 3D and 2D, of the disruption of quasi-isothermal fractal clouds immersed in supersonic winds. This work is motivated by our previous studies on uniform and turbulent magnetised clouds, which showed that the inclusion of turbulence in the initial profile of the clouds has significant effects on their evolution. In that context the goal of this paper is to study how the initial variance of the log-normal density PDF of fractal clouds affect the morphology, dynamics, and survival of clouds. To do this we compare fractal clouds characteristics of 2 regimes of turbulence, solenoidal and compressive. We summarise the conclusions drawn from our study below:

(i) *On cloud dynamics:* The dynamics of interstellar clouds immersed in supersonics winds is a function of the initial probability density function prescribed for the clouds. We find that log-normal, fractal clouds accelerate faster than uniform clouds. Aided by their intrinsic porosity, internal refracted shocks can more easily propagate through fractal clouds, thus expanding and accelerating them more effectively. Within the fractal cloud population we also find differences between solenoidal and compressive models. Compressive wind-swept clouds are more confined and, therefore, less accelerated than their solenoidal counterparts.

(ii) *On cloud survival:* We find that, owing to their higher density nuclei, compressive clouds are less prone to Kelvin-Helmholtz
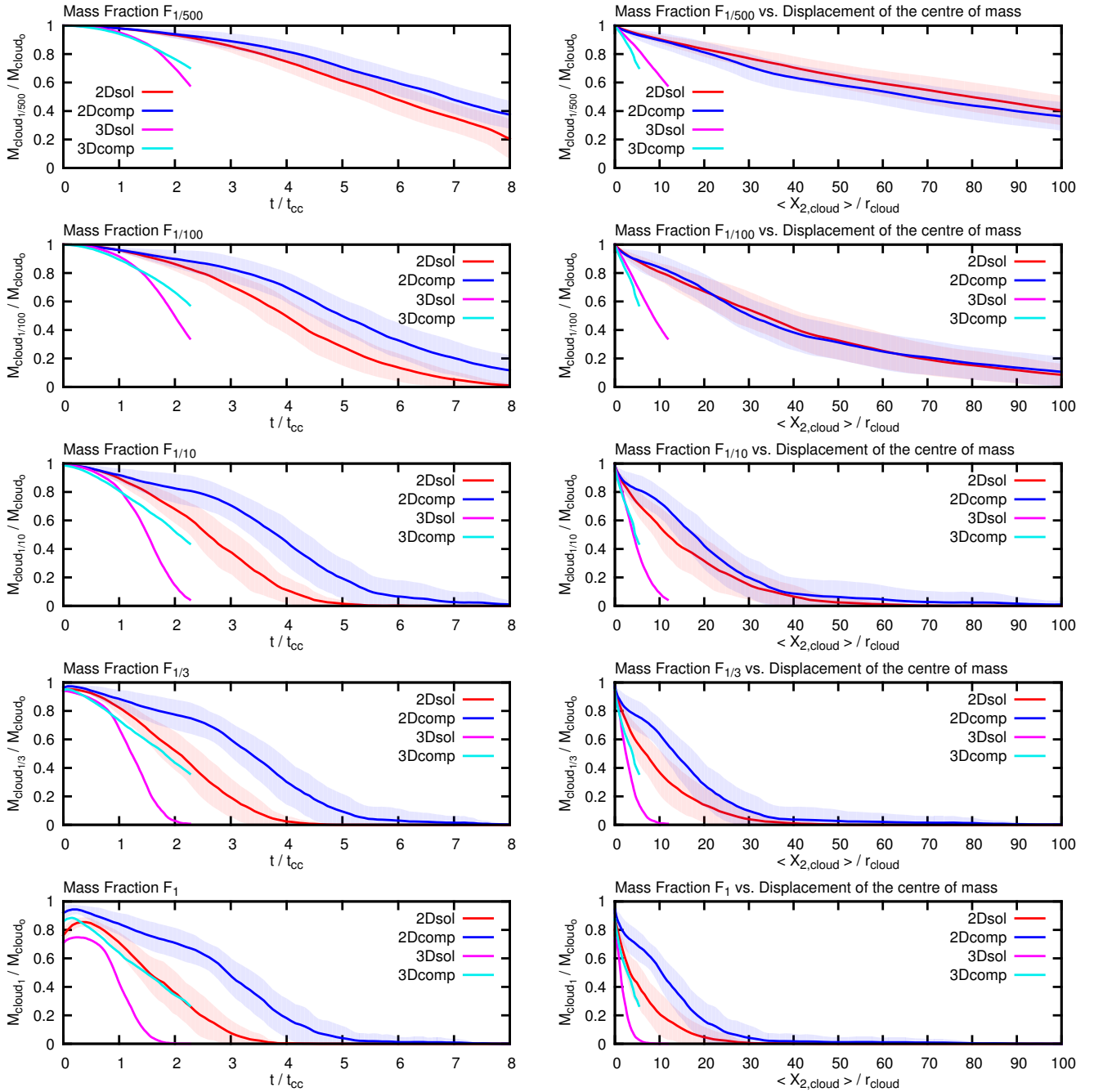
Figure 7. Time and distance evolution of the cloud mass: the lateral width (left-hand side panel), and the displacement of the centre of mass (right-hand side panel), in models m0-uni (dash-dotted line), m1-s01 (dashed line), and m2-s09 (solid line). We find that the cloud with a high initial variance is both more collimated and slower than its counterparts. The zero-variance model (i.e. the uniform cloud model) is actually the fastest of all, indicating a dependence on the variance. The smaller the variance the faster the cloud.

and Rayleigh-Taylor instabilities, so they develop less turbulence and mix with the ambient medium later than their solenoidal counterparts. This translates into compressive clouds surviving longer and reaching larger distances than solenoidal clouds before destruction (despite their slower bulk speeds). A comparison with a uniform cloud model reveals that fractal clouds are not necessarily destroyed faster than uniform clouds as previous studies indicated.

(iii) *On cloud entrainment:* The above results indicate that en-

trainment of dense gas in supersonic winds is more efficient in compressive cloud models than in solenoidal cloud models.

(iv) *On robustness:* We find that our chosen resolutions of R_{64} and R_{128} for the 3D and 2D sets adequately capture the evolution of fractal clouds for the parameter space explored in this paper. In addition, the results presented hold for 2D and 3D geometries, and for differently-seeded and distinctly-oriented fractal clouds.

(v) *On the future:* Our results indicate that compressive fractal

clouds would be ideal testbeds for future cloud acceleration studies with self-consistent velocity and magnetic fields.

REFERENCES

Alūzas R., Pittard J. M., Hartquist T. W., Falle S. A. E. G., Langton R., 2012, MNRAS, 425, 2212
Alūzas R., Pittard J. M., Falle S. A. E. G., Hartquist T. W., 2014, MNRAS, 444, 971
Banda-Barragán W. E., Parkin E. R., Federrath C., Crocker R. M., Bicknell G. V., 2016, MNRAS, 455, 1309
Banda-Barragán W. E., Federrath C., Crocker R. M., Bicknell G. V., 2018, MNRAS, 473, 3454
Brüggen M., Scannapieco E., 2016, ApJ, 822, 31
Chandrasekhar S., 1961, Hydrodynamic and hydromagnetic stability
Cooper J. L., Bicknell G. V., Sutherland R. S., Bland-Hawthorn J., 2009, ApJ, 703, 330
Fragile P. C., Murray S. D., Anninos P., van Breugel W., 2004, ApJ, 604, 74
Fragile P. C., Anninos P., Gustafson K., Murray S. D., 2005, ApJ, 619, 327
Goldsmith K. J. A., Pittard J. M., 2017, MNRAS, 470, 2427
Goldsmith K. J. A., Pittard J. M., 2018, MNRAS, 476, 2209
Gregori G., Miniati F., Ryu D., Jones T. W., 1999, ApJ, 527, L113
Gregori G., Miniati F., Ryu D., Jones T. W., 2000, ApJ, 543, 775
Grønnow A., Tepper-García T., Bland-Hawthorn J., McClure-Griffiths N. M., 2017, ApJ, 845, 69
Grønnow A., Tepper-García T., Bland-Hawthorn J., 2018, ApJ, 865, 64
Johansson E. P. G., Ziegler U., 2013, ApJ, 766, 45
Jones T. W., Kang H., Tregillis I. L., 1994, ApJ, 432, 194
Jones T. W., Ryu D., Tregillis I. L., 1996, ApJ, 473, 365
Klein R. I., McKee C. F., Colella P., 1994, ApJ, 420, 213
Kwak K., Henley D. B., Shelton R. L., 2011, ApJ, 739, 30
Li S., Frank A., Blackman E. G., 2013, ApJ, 774, 133
Mac Low M.-M., McKee C. F., Klein R. I., Stone J. M., Norman M. L., 1994, ApJ, 433, 757
Marcolini A., Strickland D. K., D'Ercole A., Heckman T. M., Hoopes C. G., 2005, MNRAS, 362, 626
McCourt M., O'Leary R. M., Madigan A.-M., Quataert E., 2015, MNRAS, 449, 2
Melioli C., de Gouveia dal Pino E. M., Raga A., 2005, A&A, 443, 495
Mignone A., Bodo G., Massaglia S., Matsakos T., Tesileanu O., Zanni C., Ferrari A., 2007, ApJS, 170, 228
Miniati F., Jones T. W., Ryu D., 1999, ApJ, 517, 242
Miyoshi T., Kusano K., 2005, J. Chem. Phys., 208, 315
Murray S. D., White S. D. M., Blondin J. M., Lin D. N. C., 1993, ApJ, 407, 588
Nakamura F., McKee C. F., Klein R. I., Fisher R. T., 2006, ApJS, 164, 477
Orlando S., Bocchino F., Peres G., Reale F., Plewa T., Rosner R., 2006, A&A, 457, 545
Orlando S., Bocchino F., Reale F., Peres G., Pagano P., 2008, ApJ, 678, 274
Pittard J. M., Parkin E. R., 2016, MNRAS, 457, 4470
Pittard J. M., Dyson J. E., Falle S. A. E. G., Hartquist T. W., 2005, MNRAS, 361, 1077
Pittard J. M., Falle S. A. E. G., Hartquist T. W., Dyson J. E., 2009, MNRAS, 394, 1351
Pittard J. M., Hartquist T. W., Falle S. A. E. G., 2010, MNRAS, 405, 821
Pittard J. M., Hartquist T. W., Dyson J. E., Falle S. A. E. G., 2011, Ap&SS, 336, 239
Poludnenko A. Y., Frank A., Blackman E. G., 2002, ApJ, 576, 832
Poludnenko A. Y., Frank A., Mitran S., 2004, ApJ, 613, 387
Raga A., Steffen W., González R., 2005, Revista Mexicana, 41, 45
Raga A. C., Esquivel A., Riera A., Velázquez P. F., 2007, ApJ, 668, 310
Scannapieco E., Brüggen M., 2015, ApJ, 805, 158
Schiano A. V. R., Christiansen W. A., Knerr J. M., 1995, ApJ, 439, 237
Schneider E. E., Robertson B. E., 2017, ApJ, 834, 144
Shin M.-S., Stone J. M., Snyder G. F., 2008, ApJ, 680, 336
Stone J. M., Norman M. L., 1992, ApJ, 390, L17
Vieser W., Hensler G., 2007, A&A, 472, 141
Xu J., Stone J. M., 1995, ApJ, 454, 172
Yirak K., Frank A., Cunningham A. J., 2010, ApJ, 722, 412
van Loo S., Falle S. A. E. G., Hartquist T. W., Moore T. J. T., 2007, A&A, 471, 213

APPENDIX A: THE WIND-CLOUD AND SHOCK-CLOUD PROBLEMS IN THE LITERATURE

Table A1 presents a summary of the parameter space explored by previous numerical studies on wind-cloud and shock-cloud interactions.

This paper has been typeset from a TEX/LATEX file prepared by the author.

Table A1. Comparison between the parameter space explored by previous authors and the present work (in Chapters 4,5, and 6). Column 1 contains the references. Column 2 provides the number of dimensions considered in their simulations and whether the models reported are purely hydrodynamic (HD), magnetohydrodynamic (MHD), or both (M/HD). Column 3 indicates the type of geometry employed to describe clouds, i.e., spherical (Sph), cylindrical (Cyl), fractal (Fra), or turbulent (Tu). Column 4 indicates the resolutions (R_x) used for the simulations in terms of the number of cells (x) per cloud radius. Columns 5, 6, 7, and 8 summarise the polytropic indices (γ), density contrasts (χ), Mach numbers ($\mathcal{M}_{wind}$), and initial plasma betas (β) reported in the references. Finally, column 9 indicates the topological structure of the magnetic field (when relevant), which could be tangled (Ta), turbulent (Tu), or aligned (Al), transverse (Tr), and oblique (Ob) with respect to the direction of the wind velocity.

(1) Reference	(2) Type	(3) Cloud	(4) Resolution	(5) γ	(6) χ	(7) $\mathcal{M}_{wind}$	(8) β	(9) Topology
Murray et al. (1993)	2D HD	Cyl	R_{25}	1.67	500, 10^3	0.25 - 1	∞	–
Jones et al. (1994)	2D HD	Cyl	R_{43}	1.67	30, 100	3, 10	∞	–
Schiano et al. (1995)	2D HD	Cyl/Sph	R_{128} - R_{270}	1.67	10 - 2000	10	∞	–
Jones et al. (1996)	2D M/HD	Cyl	R_{50}, R_{100}	1.67	10, 40, 100	10	1 - 256, ∞	Al, Tr
Miniati et al. (1999)	2D MHD	Cyl	R_{26}	1.67	10, 100	1.5,10	4	Ob
Gregori et al. (1999)	3D M/HD	Sph	R_{26}	1.67	100	1.5	4, 100, ∞	Tr
Gregori et al. (2000)	3D MHD	Sph	R_{26}	1.67	100	1.5	4, 100	Tr
Poludnenko et al. (2004)	2.5D HD	Sph	R_{128}	1.67	100	10 - 200	∞	–
Raga et al. (2005)	3D HD	Sph	R_{25}	1.0	50	2.6	∞	–
Pittard et al. (2005)	2D HD	Cyl	$R_{<32}$	1.0	≤ 350	1, 20	∞	–
Marcolini et al. (2005)	2.5D HD	Sph	R_{75}, R_{150}	1.67	100, 500	3, 6.7	∞	–
Raga et al. (2007)	3D HD	Sph	R_{76}	1.67	10	242	∞	–
Vieser & Hensler (2007)	2.5D HD	Sph	R_{28} - R_{33}	1.67	1 - 10^4	0.3	∞	–
Cooper et al. (2009)	3D HD	Fra	R_6 - R_{38}	1.67	630 - 1260	4.6	∞	–
Kwak et al. (2011)	2D HD	Sph	$R_{<64}$	1.67	10^3	0.6 - 2	∞	–
McCourt et al. (2015)	3D MHD	Sph	R_{32}	1.67	50	1.5	0.1 - 10	Ta
Scannapieco & Brüggen (2015)	3D HD	Sph	R_{32} - R_{128}	1.67	300 - 10^4	0.5 - 11.4	∞	–
Brüggen & Scannapieco (2016)	3D HD	Sph	R_{32} - R_{96}	1.67	300 - 10^4	0.99 - 11.4	∞	–
Banda-Barragán et al. (2016)	3D M/HD	Sph	R_{128}	1.67, 1.1	10^3	4, 4.9	10, 100, ∞	Al, Tr, Ob
Goldsmith & Pittard (2017)	2.5D HD	Sph	R_{128}	1.67	10	10	∞	–
Grønnow et al. (2017)	3D MHD	Sph	R_{16} - R_{32}	1.67	500, 2500	1.5, 3.5	–	Tr
Goldsmith & Pittard (2018)	2.5D HD	Sph	R_{128}	1.67	10^3	10	∞	–
Grønnow et al. (2018)	3D MHD	Sph	R_{16} - R_{32}	1.67	500, 2500	1.5, 3.5	–	Tr
Banda-Barragán et al. (2018)	3D MHD	Tu	R_{128}	1.67	10^3	4	0.04 - 100	Tu
Stone & Norman (1992)	3D HD	Sph	R_{60}	1.67	10	10	∞	–
Klein et al. (1994)	2.5D HD	Sph	R_{60} - R_{240}	1.67, 1.1	3 - 400	10 - 10^3	∞	–
Mac Low et al. (1994)	2.5D MHD	Cyl, Sph	R_{25} - R_{240}	1.67	10	10 - 100	0.01, 1	Al, Tr
Xu & Stone (1995)	3D HD	Sph	R_{11} - R_{64}	1.67	10	10	∞	–
Poludnenko et al. (2002)	2D HD	Cyl	R_{32}	1.67	500	10	∞	–
Fragile et al. (2004)	2D HD	Cyl	R_{200}	1.67	10^3	5 - 40	∞	–
Fragile et al. (2005)	2D MHD	Cyl	R_{100}, R_{200}	1.67	10^3	10	1 - 100	Al, Tr
Melioli et al. (2005)	3D HD	Sph	R_{32}	1.67	100, 500	7	∞	–
Nakamura et al. (2006)	2.5/3D HD	Sph	R_{30} - R_{960}	1.67, 1.1	10, 100	1.5 - 10^3	∞	–
Orlando et al. (2006)	2/3D HD	Sph	R_{105}, R_{132}	1.67	10	30, 50	∞	–
van Loo et al. (2007)	2.5D MHD	Sph	R_{640}	1.67	45	1.5 - 5	1	Al
Orlando et al. (2008)	2.5D M/HD	Sph	R_{132} - R_{528}	1.67	10	50	1 - 100	Al, Tr
Shin et al. (2008)	3D MHD	Sph	R_{120}	1.67	10	10	0.5 - 10	Al, Tr, Ob
Pittard et al. (2009)	2.5D HD	Sph	R_{16} - R_{256}	1.67	10 - 10^3	10	∞	–
Pittard et al. (2010)	2.5D HD	Sph	R_{128}	1.67	10-10^3	1.5 - 10	∞	–
Yirak et al. (2010)	2.5D HD	Sph	R_{12} - R_{1536}	1.67	100	50	∞	–
Pittard et al. (2011)	2.5D HD	Sph	R_{128}	1.67	10^3	1.5, 3	∞	–
Alūzas et al. (2012)	2/3D HD	Cyl, Sph	R_8 - R_{256}	1.67	10 - 10^3	1.5 - 10	∞	–
Johansson & Ziegler (2013)	3D MHD	Sph	R_{100}	1.67	100	30	1 - 10^3	Al, Tr
Li et al. (2013)	3D MHD	Sph	R_{54}	1.67	100	10	0.25, 1	Se
Alūzas et al. (2014)	2D HD	Cyl	R_{32}, R_{128}	1.67	100	3	0.5 - 5	Al, Tr, Ob
Pittard & Parkin (2016)	2.5/3D HD	Sph	R_8 - R_{128}	1.67	10 - 10^3	1.5 - 10	∞	–
Schneider & Robertson (2017)	3D HD	Tu	R_{32} - R_{128}	1.67	19 - 190	5	∞	–